High temperature creep flow and damage properties of the weakest area of 9Cr1Mo-NbV martensitic steel weldments

Vincent Gaffard, Anne-Françoise Gourgues-Lorenzon, Jacques Besson

HAL Id: hal-00136781
https://hal.science/hal-00136781

Submitted on 23 Apr 2007

High Temperature Creep Flow and Damage Properties of the Weakest Area of 9Cr1Mo–NbV Martensitic Steel Weldments

V. GAFFARD, A. F. GOURGUES-LORENZON and J. BESSON

Ecole Nationale Supérieure des Mines de Paris, Centre des Matériaux, UMR CNRS 7633 BP 87, 91003 Evry Cedex, France.
E-mail: anne-francoise.gourgues@ensmp.fr

In the present study, creep flow and damage behaviour of modified P91 steel weldments are investigated. Premature creep failure of weldments (with respect to base metal) occurs in the intercritical heat affected zone (ICHAZ). This microstructure is reproduced by thermal simulation applied to blanks cut from the base metal. Metallurgical investigations of what happens during the welding cycle show that the weakest part of the heat affected zone is heated slightly below complete austenitisation, with little (if any) carbide dissolution. During the post-weld heat treatment, extensive recovery is allowed by carbide coarsening. The intrinsic creep behaviour of the resulting microstructure is experimentally determined under controlled constraint conditions. The welding cycle strongly decreases the creep strength by increasing the creep strain rate, but not necessarily by decreasing the ductility, at least for lifetimes up to 3 500 h.

KEY WORDS: 9Cr1Mo–NbV martensitic steel; intercritical heat affected zone; Gleeble 1 500 thermal-mechanical simulator; High temperature creep flow and damage.

1. Introduction

9Cr1Mo–NbV martensitic steels are candidates as structural materials for supercritical and ultra-supercritical power plants. They exhibit suitable weldability[1] due to good thermal conductivity and low thermal expansion but welding of high thickness components is still rather difficult. Therefore, low input energy levels, $<2200 \, \text{J mm}^{-1}$, are generally required.[2] In addition, the welding operation leads to the modification of the base metal microstructure in the so-called heat affected zone (HAZ). Thermal cycles experienced in the HAZ are usually characterised by a peak temperature, T_{peak}, and a cooling time between 800°C and 500°C, $\Delta t_{800 \rightarrow 500}$. They lead locally to phase transformations so that the HAZ in these steels is classically divided into three main areas:

1. The coarse grained heat affected zone (CGHAZ) exhibits a higher former austenite (γ) grain size ($T_{peak} \gg Ac_3$).

2. The fine grained heat affected zone (FGHAZ) exhibits a small former austenite grain size, as T_{peak} is just above Ac_3.

3. The intercritical heat affected zone (ICHAZ) corresponds to $Ac_1 < T_{peak} < Ac_3$. In this area, the $\alpha \rightarrow \gamma$ phase transformation only partially proceeds during the thermal cycle.

Just near the HAZ, the over-tempered base metal area corresponds to T_{peak} just below Ac_1 which leads to over-ageing of the base metal.[3]

The microstructural changes in the HAZ are of great importance, as the creep strength of the weldment is lower than that of the base metal and this is attributed to the HAZ, where creep failure occurs. The HAZ area which governs the creep failure has already been identified.[4] A fracture mechanism map has been proposed,[4] where the evolution of damage mechanism in weldments from intragranular to intergranular fracture is represented. These results are to be confirmed by the present study. Premature failure of weldments could be related to two phenomena:

1. There is a weakness in the weldment, linked to the lower creep strength of the HAZ: this is a metallurgical problem.

2. The microstructural heterogeneity obviously leads to complex loading states and constraint effects: this is a mechanical problem.

The present study is concerned with the first point *i.e.* determining the intrinsic creep flow and damage properties of the weakest HAZ. To do so, special attention was focused on avoiding constraint effects induced by microstructural heterogeneity. A method to represent several microstructural states of the HAZ with thermal simulations was first validated using various metallurgical investigation techniques. Then, a welding thermal cycle corresponding to the weakest HAZ was chosen, allowing to machine various kinds of specimens having the same microstructure as the weakest HAZ. All specimens were notched, in order to localise loading in the microstructure under interest, with controlled constraint effects due to the notch geometry only. This point is especially important as in previous studies,[5,6] uniaxial creep tests were carried out on smooth specimens so that several microstructures were tested at the same time; due to the microstructural inhomogeneity, the loading state

Table 1. Chemical compositions of base and filler metals (wt%).

	C	Si	Mn	P	S	Al	Cr	Ni	Mo	V	Nb	N	Cu
Base Metal	0.09	0.31	0.41	0.014	0.005	0.016	8.56	0.26	0.92	0.21	0.065	0.042	/
Filler Metal	0.09	0.37	0.41	0.028	0.013	0.07	8.44	0.27	0.92	0.24	/	0.038	0.04

in the microstructure of interest was not known, just as for cross-weld specimens. The key point of the present study is thus to determine the properties of the weakest HAZ while eliminating, as much as possible, the constraint effects due to the surrounding materials.

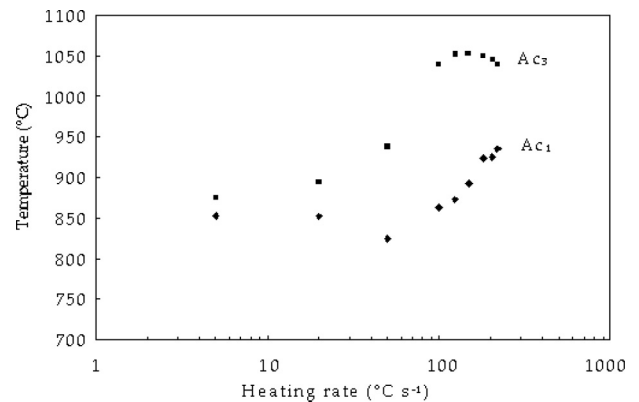## 2. Material and Experimental Procedures

2.1. Materials

The study focuses on a V-shaped, circumferentially welded joint of two pipes of 295 mm in outer diameter and 55 mm in thickness. It was fabricated by submerged metal arc welding in seventeen runs followed by a post weld heat treatment (PWHT) of 2 h at 760°C. The base metal is a tempered, modified P91 martensitic steel (see **Table 1** for chemical composition). Its microstructure consists of lath martensite packets with $M_{23}C_6$ (100 nm in mean size) and MX precipitates. The filler metal has nearly the same chemical composition as the base metal (Table 1).

2.2. Simulation of Welding Thermal Cycles

Welding thermal cycles were applied by using a Gleeble 1 500 thermal-mechanical simulator capable of heating specimens by Joule effect at very high heating rates, corresponding to those encountered in welding conditions (*i.e.* 100 to 250°C·s^{-1}). The temperature is controlled by a thermocouple spot welded onto the specimen surface. Round bars of 5 mm in diameter were used to optimise the thermal cycle and 12 mm round blanks were treated and used to machine mechanical testing specimens respectively. For each of these two geometries, the closed-loop parameters of the Gleeble 1 500 simulator were carefully adjusted in order to ensure an uncertainty lower than 2°C for the value of T_{peak} and smaller than 1 s for the value of the cooling parameter $\Delta t_{800 \rightarrow 500}$. For specimens of 5 mm in diameter, phase transformations were continuously monitored using *in-situ* dilatometric measurement of the specimen diameter. To prevent from extensive oxidation of the specimen, heat treatments were performed under primary vacuum (0.1 Pa). Phase transformations monitoring is of highest importance, as both austenite start and end transformation temperatures (respectively Ac_1 and Ac_3) and the properties of the austenite phase strongly depend on the heating rate.[7] In the present study, when increasing the heating rate from 5 to 200°C s^{-1}, Ac_1 and Ac_3 temperatures increase by more than 150°C (**Fig. 1**). Moreover, the temperature range of the intercritical domain (*i.e.* Ac_3–Ac_1) also increases from 25°C to 100°C. In the following, Ac_1 and Ac_3 temperatures are thus mentioned according to the corresponding heating rate.

2.3. Mechanical Tests

Creep tests on cross-weld specimens were carried out on smooth round tensile bars (SC specimens) cut along the axial direction of the pipe with a gauge length of 36 mm

Fig. 1. Effect of the heating rates on Ac_1 and Ac_3 temperatures (dilatometry, the accuracy of the measured temperatures is ±5°C).

and a gauge diameter of 5 mm. The specimens were machined so that the base metal, the HAZ and the weld metal could be tested at the same time. These tests allowed to evaluate the difference in creep lifetime between the base metal and the weldment and to determine the rupture location in weldments.

Creep tests were also carried out on simulated HAZ microstructures. To do so, the round blanks of 12 mm in diameter were first applied the weld thermal cycle corresponding to the weakest HAZ (see Sec. 5.3) followed by the actual PWHT *i.e.* 760°C for 2 h. From Vickers hardness measurements and for the chosen operating conditions, the Gleeble heat treatment is homogenous within a 7 mm wide area centred on the thermocouple. Therefore, creep and tensile specimens were notched to localise stress and strain in the centre of the thermally treated area. To determine tensile and creep flow properties of the simulated HAZ, a smoothly notched tensile specimen (NT) was designed with a maximum diameter of 4 mm, a minimum diameter of 3 mm and a notch radius of 5 mm and a creep specimen (NC5.0) was designed with a maximum diameter of 6 mm, a minimum diameter of 3 mm and a notch radius of 5 mm. All creep tests on NC5.0 specimens were performed until failure except for one complementary test with load varying with steps (50 MPa, 60 MPa and 70 MPa), which allowed to investigate creep flow properties in the low stress creep regime.

As the stress triaxiality ratio, *i.e.* the ratio between the local hydrostatic pressure and the local von Mises equivalent stress, may play a key role in damage mechanisms, two other types of round U-notched specimens (NC4.0, NC1.2) with a maximum diameter of 6 mm, a minimum diameter of 3 mm and a notch radius of respectively 4 mm and 1.2 mm, were designed. Two types of round V-notched bars (NC0.25), which allow to obtain stable crack propagation and to test the effect of an even higher triaxiality ratio, were also used. The first and second types NC0.25-1 (respectively NC0.25-2) have a maximum diameter of 8 mm, a mini-

mum diameter of 5 mm (resp. 4 mm) and a notch radius of 0.25 mm.

All creep tests were carried out at 625°C (898 K) for up to 10 000 h under constant applied load in controlled laboratory atmosphere (20°C±2°C and 50% relative humidity). The load was applied using dead weights for SC specimens and using an electrical mechanical testing machine for NT and NC specimens. The temperature was monitored using three thermocouples spot welded onto the specimen surface; the temperature gradient between top and bottom ends did not exceed 2°C. The total elongation was continuously measured by a linear variable differential transducer with a sensitivity of 1 μm.

2.4. Metallurgical Investigations

Light optical observations after Villela etching and scanning electron microscopy (SEM) investigations using backscattered electron (BSE) imaging after colloidal silica polishing were carried out. The precipitation state was characterised using the carbon extraction replica technique to determine both the size distribution (by image analysis) and the chemical composition of precipitates (by using X-Ray energy dispersive spectroscopy (EDS)) in a Zeiss DSM 982 SEM equipped with a field emission gun (FEG-SEM). Transmission electron microscopy (TEM) investigations were performed in a 200 kV JEOL 2000FX microscope. Thin foils were prepared by mechanical polishing followed by double jet electrolytic thinning. A 45% butoxyethanol, 45% acetic acid and 10% perchloric acid solution was used at 0°C under 40 V. Electron backscatter diffraction (EBSD) analysis was conducted in the FEG-SEM at 20 kV with the specimen tilted by 70° after polishing with colloidal silica. It allows to quantitatively investigate the microstructural state and the evolution of grain boundary misorientations over large areas.

X-Ray diffraction θ–2θ spectra were collected at room temperature in the range $(2\theta)=96°$ to 126° by steps of 0.032° with a counting time of 0.6 s per step. A diffractometer with Co-K$_\alpha$ radiation having a wavelength of 0.1788 nm and a Fe-K$_\beta$ filter were used together with an entry slit of 0.3° and a linear detector of type Elphyse, which was calibrated using silicon as a reference sample.

3. Simulation of HAZ Microstructures and Determination of Conditions to Reproduce the Weakest HAZ of the Welded Joints

The thermal cycles experienced in the HAZ were first modelled to determine the thermal cycles to apply on laboratory specimens in the thermal-mechanical simulator. Then, specimens were treated with various weld thermal cycles in order to validate the thermal model parameters, by comparison with real microstructures. Both results of creep tests on cross-weld specimens and metallurgical investigations of thermally treated specimens were used to determine the thermal cycle corresponding to the weakest HAZ.

3.1. Modelling the Welding Thermal Cycles

The calculations of welding thermal cycles were based on the Rosenthal model of thermal dissipation[8] specifically designed for the case of arc welding and later simplified by

Table 2. Physical constants and welding parameters for the thermal model.

Thermal conductivity	$\Gamma = 28$ Wm^{-1}K^{-1} (at 250°C)
Heat input energy	H = 1296 Jmm^{-1}
Arc displacement rate	$v_a = 2.6 \cdot 10^{-3}$ ms^{-1}.
Preheat temperature	T$_0$ = 250 °C
Thickness of the component	w = 55 mm
Cooling parameter	$\Delta t_{800\to500}$ = 16 s
Heat source position	4.5 mm from the fusion line and 10 mm under the top surface

Table 3. Heat cycles performed.

Distance from the fusion line	Peak temp.	Heating rate	Specificity
1.50 mm	1200°C	218°C s^{-1}	A$_{c3}$ < T$_{peak}$
2.00 mm	1128°C	204°C s^{-1}	A$_{c3}$ < T$_{peak}$
2.50 mm	1056°C	181°C s^{-1}	A$_{c3}$ ≈ T$_{peak}$
3.00 mm	995°C	158°C s^{-1}	A$_{c1}$ < T$_{peak}$ < A$_{c3}$
3.25 mm	986°C	155°C s^{-1}	A$_{c1}$ < T$_{peak}$ < A$_{c3}$
3.50 mm	960°C	152°C s^{-1}	A$_{c1}$ < T$_{peak}$ < A$_{c3}$
3.75 mm	936°C	148°C s^{-1}	A$_{c1}$ < T$_{peak}$ < A$_{c3}$
4.00 mm	911°C	128°C s^{-1}	A$_{c1}$ < T$_{peak}$ < A$_{c3}$
4.15 mm	885°C	126°C s^{-1}	A$_{c1}$ < T$_{peak}$ < A$_{c3}$
4.20 mm	877°C	124°C s^{-1}	T$_{peak}$ < A$_{c1}$
4.50 mm	860°C	121°C s^{-1}	T$_{peak}$ < A$_{c1}$

Rykalin.[9] This model does not allow to represent the effects of multiple runs but was chosen for its simplicity and by assuming that for a given run, the following one only acts as a short term tempering treatment. As previously shown,[10] a three dimensional formulation must be used because of the 55 mm thickness of the pipe.

The model postulates that the heat input energy is mainly dissipated by conduction. The annealing time at T_{peak} is very short (typically<2 s). The cooling parameter $\Delta t_{800\to500}$ mainly depends on the heat input energy and little on T_{peak} and its value does not strongly affect the austenite to martensite phase transformation, thus, it was set constant. Material constants shown in **Table 2** were taken from Refs. 11), 12). Other parameters, such as the arc displacement rate, the preheat temperature and the heat input energy (taking into account the efficiency of the process) are given by the process. Only one parameter had to be experimentally determined: the location of the heat source. It was evaluated by microstructural observation of the weld metal, as the columnar solidification grains had grown along the direction of the thermal gradient. Note that the cooling parameter $\Delta t_{800\to500}$ does not exceed 31 s, in order to avoid formation of primary ferrite.[2]

3.2. Comparison between Real and Simulated HAZs

The ability of the thermal model to be used to reproduce various microstructural states of the HAZ was investigated. Several treatments were calculated using the above model and then applied to round bars to simulate the thermal cycles experienced by the material at various distances from the fusion line and involving heating in the α, $\alpha+\gamma$ and γ temperature ranges. For every thermal cycle of **Table 3**, two specimens were heat treated and one of them was then given the PWHT of 2 h at 760°C for comparison with the actual welded joint. Thus, the properties of the simulated microstructures could be evaluated both before and after PWHT. Vickers hardness values of the simulated, PWHT-tempered microstructures are very close to those measured
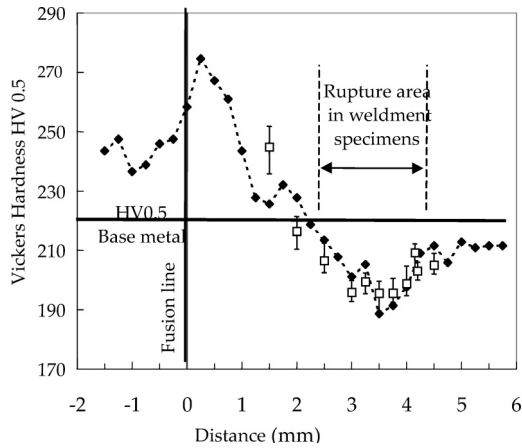
Fig. 2. Hardness comparison after PWHT: full symbols=welded joints and open symbols=simulated HAZ.

Fig. 3. Evolution of phase transformations (dilatometry).

Fig. 4. Difference in the martensite start temperatures as a function of the thermal cycle.

Fig. 5. Vickers hardness of simulated microstructures before PWHT.

in corresponding areas of the tempered weldment (**Fig. 2**). Therefore, it was assumed that the distance to the fusion line is a relevant parameter to evaluate, by using the model, the thermal cycle locally experienced by the HAZ microstructure.

3.2.1. Microstructure of the Matrix after the Simulated Welding Cycle

The phase transformations were first investigated during heating and cooling by using the dilatometry results. The values of Ac_1 and Ac_3 were determined as a function of the heating rate with an accuracy of $\pm 5°C$ (Fig. 1). Two phase transformations were evidenced on all cooling curves, leading to the definition of two M_s temperatures M_{s1} and M_{s2} (**Figs. 3** and **4**). This phenomenon had already been observed[13] in a 0.3C–13Cr steel and attributed to the inhomogeneity in the austenite phase due to partial dissolution of carbides during heating, i.e., the matrix is locally enriched in carbon and chromium atoms that are released by dissolved precipitates.

From Table 3, among all performed heat cycles, those with $885°C \leq T_{peak} < 1\,056°C$ correspond to intercritical heating. This was confirmed by hardness measurements in the as-welded condition as shown in **Fig. 5**, where the hardness abruptly increases for these thermal cycles, due to martensite freshly formed during cooling of the partially transformed austenite. A rule of mixtures was used to calculate the percentage of martensite both transformed during heating and formed between the two M_s temperatures. Figure 3 confirms that the $\alpha \rightarrow \gamma$ phase transformation begins for weld thermal cycles with T_{peak} slightly below 900°C and is nearly complete for T_{peak} reaching 1 100°C. These results are consistent with a previous study[14] showing that 80% of the $\alpha \rightarrow \gamma$ phase transformation has proceeded for T_{peak}=920°C for a comparable value of the heating rate (see Table 3). Figure 3 also shows that the percentage of martensite transformation between M_{s1} and M_{s2} reaches a maximum value of 20% for T_{peak} around 1 000°C.

Freshly formed martensite could not be distinguished from untransformed martensite by SEM investigations, even in the as welded condition, so that dilatometric results could not be confirmed by direct observations. No retained austenite between the martensite laths[15,16] could be evi-
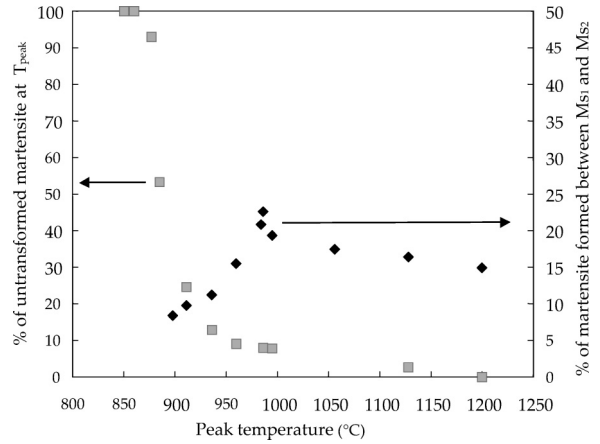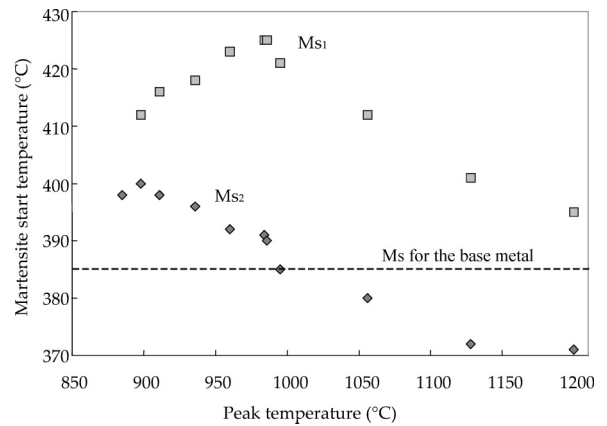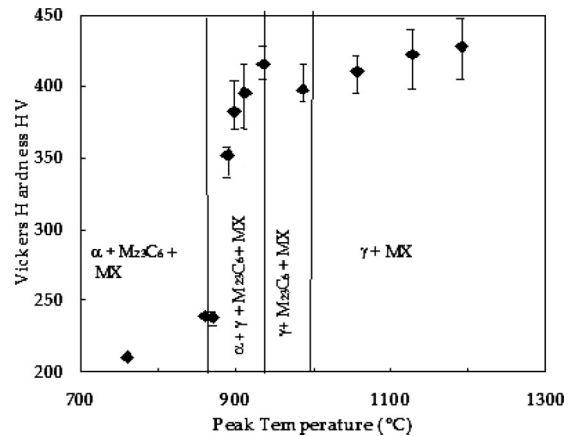
denced here by either high resolution SEM investigations or X-Ray diffraction analysis.

The evolution of M_{s1} and M_{s2} versus T_{peak} is plotted in Fig. 4. The increase in the values of M_s with T_{peak} can be attributed to easier nucleation (due to more numerous austenite grain boundaries) but also, and more probably, to a lower carbon content in the solid solution.[17] When decreasing the carbon content from 0.16 to 0.002 wt% in a 9Cr3W steel, the martensite start temperature increases by 100°C.[18] Here, the maximum variation between M_{s1} and

M_{s2} occurs for $T_{peak} \approx 990°C$. For $T_{peak}=1\,200°C$ the average value of M_s is nearly the same as that of the base metal. The shape of the M_s vs. T_{peak} curves for T_{peak} in the intercritical domain is difficult to explain, as both the $\alpha \rightarrow \gamma$ phase transformation and the dissolution of $M_{23}C_6$ carbides are only partial. Thus, for a better understanding, the evolution of the precipitation state during welding thermal cycles was also investigated.

3.2.2. Evolution of Precipitates during the Simulated Welding Cycle

Two types of carbides, MX and $M_{23}C_6$, were observed in the initial state. In the present study, the evolution of MX (namely, V(C, N) and Nb(C, N)) precipitates in the simulated and tempered microstructures was not investigated. However, it can be assumed that in the ICHAZ, primary MX stay during weld thermal cycles as their dissolution temperature is higher than 1 100°C.[5,19] For intercritical heat treatments of Table 3, both the peak temperature lower than of 1 100°C and the high heating rate do not allow dissolution of these precipitates. During the rapid thermal cycle, primary MX precipitates could only grow or coarsen a little.[20] Finer MX precipitates were already globular and incoherent with the matrix in the base metal, so that no spheroidisation was expected to occur during the thermal cycle.[6]

Carbide dissolution during heating is not well understood. Several authors[21–24] considered that the dissolution of $M_{23}C_6$ carbides only occurs after the main part of the $\alpha \rightarrow \gamma$ phase transformation has proceeded. Others[25] proposed a slightly different dissolution sequence for Fe–Cr–Mo steels with high C and Mo contents. In fact, the dissolution sequence of $M_{23}C_6$ carbides strongly depends on the chemical composition. Here, the occurrence of carbide dissolution with respect to the $\alpha \rightarrow \gamma$ phase transformation was experimentally investigated by looking at hardness values of simulated microstructures before PWHT (Fig. 5) more closely. A small drop in hardness for $T_{peak} \approx 990°C$ is evidenced. It does not correspond to the presence of retained austenite. Following the previous work of Sanderson,[26] it could possibly be related to carbide dissolution. To try to confirm this, the amount of carbon dissolved in the martensitic matrix in the as-welded condition was investigated by X-Ray diffraction. The martensite tetragonality strongly depends on the carbon content in the solid solution. A classically used relationship for the binary Fe–C system[27,28] is:

$$\frac{c}{a} = 1.000 + 0.045[C]_{ss} \quad \text{.......................(1)}$$

where c and a are the martensite lattice parameters and $[C]_{ss}$ is the carbon content in the martensite solid solution in mass%. However, despite the high accuracy of the measurements (better than 0.001 nm), the change in the lattice parameters due to the tetragonality of martensite was presumably lower than the detection limit.

On the other hand, the lower M_s temperature (M_{s2}) starts to be lower than the M_s temperature of the base metal itself for peak temperatures higher than about 1 000°C (Fig. 4). This suggests that some carbides could start to dissolve into austenite for higher peak temperatures. This result is consistent with literature data[29,30] obtained by TEM measurements of the carbide lattice parameters together with mass

conservation, showing that in such thermal conditions, significant dissolution of carbides only starts for peak temperatures higher than 1 000°C. This slow dissolution of carbides is due to the fast heating and cooling rates in the weld thermal cycles and to carbon trapping in MX precipitates.

From the investigations presented above one can conclude that:

1. The weld thermal cycles whose peak temperature: 885°C $< T_{peak} <$ 1056°C are intercritical treatments.
2. $M_{23}C_6$ carbides probably start to dissolve significantly for $T_{peak} >$ 1 000°C but part of the martensite resulting from the $\gamma \rightarrow \alpha$ transformation after heating at $T_{peak} <$ 1 000°C still exhibits a strong lack in carbon.
3. In the conditions of the weld thermal cycles, the primary MX carbides do not dissolve, at least for $T_{peak} <$ 1 100°C and probably little grow or coarsen.

3.2.3. Effects of the PWHT

Several studies of the base metal have shown that the microstructural stability of 9Cr1Mo–NbV steels, especially under high temperature ageing and creep conditions, strongly depends on the pinning of dislocations and grain boundaries by a fine distribution of carbides.[31–34] Both a large carbide size and a low carbon content promote rapid softening of martensite during a high temperature tempering treatment.[35]

The hardness profile of Fig. 2 shows that in the CGHAZ (i.e. between 1 and 2 mm far from the fusion line), the hardness is rather high (20 points higher than that of the base metal) as the precipitation of new strengthening carbides occurs during the PWHT, and as the base metal is actually given two tempering treatments whereas the CGHAZ is given only one, namely, the PWHT.

On the contrary, in the ICHAZ (i.e. between 3 and 4 mm far from the fusion line), the hardness is lower by 20 points than that of the base metal, which indicates softening of the material, attributed to lath martensite recovery[36] or to precipitate growth.[20] Both phenomena are closely related due to the pinning effect of carbides.[3] SEM investigations performed both on our as-simulated and tempered microstructures confirmed that extensive lath recovery occurs during the PWHT for weld thermal cycles with a peak temperature ranging from 880°C to 1 050°C i.e. for intercritically treated microstructures. This is consistent with observations in the corresponding areas of the welded joint.

The evolution of precipitates was also investigated. Carbon extraction replicas were analysed for the simulated and tempered microstructures and the corresponding zones of the weldment. The comparison of precipitate size distributions evidenced a difference of only 10 to 20 nm in the average size of $M_{23}C_6$ carbides between simulated and real microstructures. The mean size of carbides after PWHT is larger than 200 nm in the ICHAZ, i.e. twice the size measured in the base metal. The evolution of $M_{23}C_6$ carbide population observed in the present study is consistent with previous results[18] showing that when the carbon content is lowered, the $M_{23}C_6$ carbides exhibit a larger size and are less in number. Extensive lath recovery probably results from a lack in dissolved carbon and from rapid coarsening of the $M_{23}C_6$ carbides not dissolved during the weld thermal cycle.

Table 4. Typical thermal treatments used to simulate microstructures of the weak HAZ (Note that when heating and cooling rates are not given, thermal treatment are probably performed in conventional furnaces).

Ref.	Peak temperature	Heating rate	Cooling rate	PWHT
37	850-1000°C	60-70°C s⁻¹	15-90°C s⁻¹	2.2 h - 740°C
38	940°C	*Not given*	*Not given*	4.0 h – 774°C
39	900 – 960°C	150°C s⁻¹	$\Delta t_{800\to 500} = 21$ s	12.0 h - 730°C
40	850 °C	*Furnace (heating in 6 minutes and dwell of 5 minutes followed by air cooling)*		12.0 h – 730°C
6	900 °C	270°C s⁻¹	$\Delta t_{800\to 500} = 30$ s	8.5 h – 740°C
5	900 – 1100°C	*Not given*	$\Delta t_{800\to 500} = 10$ s	1.0 h – 750°C
42	900 – 1000°C	*Not given*	*Not given*	2.0 h – 760°C
41, 43	920°C	4°C s⁻¹	*Not given*	4.5 h – 740°C
44	850°C	*Furnace (dwell of 20 minutes followed by air cooling)*		2.0 h – 760°C

The PWHT temperature plays a key role in martensite recovery. An alternative PWHT of 2 h at 600°C was performed on several as-simulated ICHAZ microstructures. In all cases, SEM investigations and hardness measurements revealed that lath martensite had not softened during that alternative PWHT, consistently with literature data.[15]

3.3. Choice of a Weld Thermal Cycle

Many authors performed heat treatments in order to reproduce the weakest microstructure of the HAZ, using either a conventional furnace or a welding simulator (**Table 4**). Most of them chose a thermal cycle corresponding to an intercritical treatment, *i.e.* on a purely metallurgical basis. However, Tsuchida *et al.*[6] and Otoguro *et al.*[5] carried out high temperature creep tests on several simulated microstructures to determine which one had the lowest creep strength. The need to superimpose a mechanical loading on the weld thermal cycle simulation to promote martensite softening during PWHT has already been addressed[45]; the authors found that final microstructures obtained by a thermal treatment under stress near Ac_1 and a stress free thermal treatment near Ac_3, respectively, were similar.

In the present study, the weld thermal cycle corresponding to the weakest HAZ was chosen using both metallurgical criteria and a geometrical-mechanical criterion (location of rupture in cross-weld specimens, characterised by the initial distance of the involved microstructure to the fusion line), as it was shown in Sec. 3.2 that the thermal model well reproduces the corresponding zone in the real weldment.

First, creep tests on cross-weld SC specimens were carried out. The initial values of engineering stresses ranged from 100 to 50 MPa (corresponding to lifetimes from 300 h to 10 000 h), and from 120 to 90 MPa (corresponding to lifetimes from 800 to 7 000 h) for the weldment and the base metal, respectively. Creep results of the present study are consistent with literature data[3] The creep lifetime of the weldment is more than ten times lower than that of the base metal for a given applied engineering stress (*e.g.* 300 h *vs.* 3 500 h under 100 MPa), which corresponds to a decrease in creep strength by 30%. Cross-sectional SEM investigations of weldment specimens evidenced that rupture occurs in the ICHAZ near the base metal (*i.e.* more than 2.5 mm far from the fusion line, see Fig. 2) parallel to the fusion line (type IV rupture). Damage is mainly located in the ICHAZ (*i.e.* over a distance of 2 mm) but cavities are also detected in all the HAZ and in the over-tempered base metal. Similar observations are reported in the temperature

range 575–650°C.[4,29,46] Therefore, it is assumed that the thermal cycle corresponding to the weakest HAZ is characterised by a peak temperature: $885°C < T_{peak} < 1060°C$ (*i.e.* in the intercritical domain).

The choice of one of the intercritical cycles was based on metallurgical considerations. Second phase particles have a pinning effect on grain boundaries and dislocations. So, $M_{23}C_6$ carbide coarsening and changes in MX precipitation behaviour in the freshly formed martensite[20,29] promote faster kinetics of creep recovery. Large carbides are also likely to be preferential sites for creep cavity nucleation as already evidenced for the base metal.[47] Taking into account the results of the previous section, the weld thermal cycle was chosen as the cycle for which the $\alpha \to \gamma$ phase transformation is almost completed, while dissolution of $M_{23}C_6$ has not yet occurred during heating. The characteristics corresponding to this cycle are given in Table 3.

The chosen peak temperature of 986°C is slightly higher than the literature values given in Table 4. Note, however, that Otoguro *et al.*[5] showed that the weakest simulated microstructure was that with $T_{peak}=900°C$ for short term creep tests and that with $T_{peak}=1000°C$ for long term creep tests. Matsui *et al.*[43] also showed that the weld thermal cycle corresponding to the weakest HAZ exhibits a peak temperature just below Ac_3.

3.4. Metallurgical Validation of the Chosen Thermal Cycle

The TEM comparison between simulated and real microstructures for the chosen cycle is shown in **Fig. 6**. The two microstructures exhibit the same characteristics in terms of matrix morphology (*i.e.* low dislocation density and small equiaxed grains) and precipitation state. These observations were confirmed by EBSD analysis showing the size and morphology of grains (see **Fig. 7**). The grain boundary misorientation distribution, which plays a significant role in the creep behaviour, is dominated in both microstructures by low angle boundaries (misorientations between 5° and 15°). This is consistent with the occurrence of lath recovery during the PWHT. It will be shown in the following section that creep damage mechanisms of real and simulated HAZ microstructures are also similar.

4. Tensile, Creep Flow and Damage Properties of the Simulated ICHAZ Microstructure at 625°C

4.1. Tensile Properties at 625°C

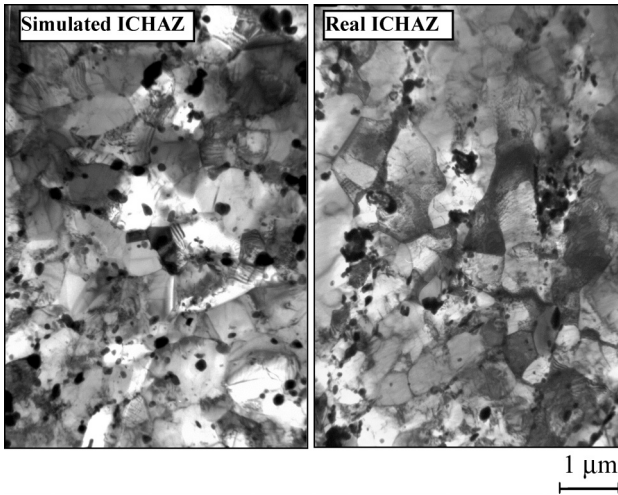Stress–strain curves show a strong strain rate effect on

Fig. 6. Thin foil TEM investigations: Comparison of real and simulated intercritical heat affected zone (T_{peak}=986°C) microstructures (bright field images).
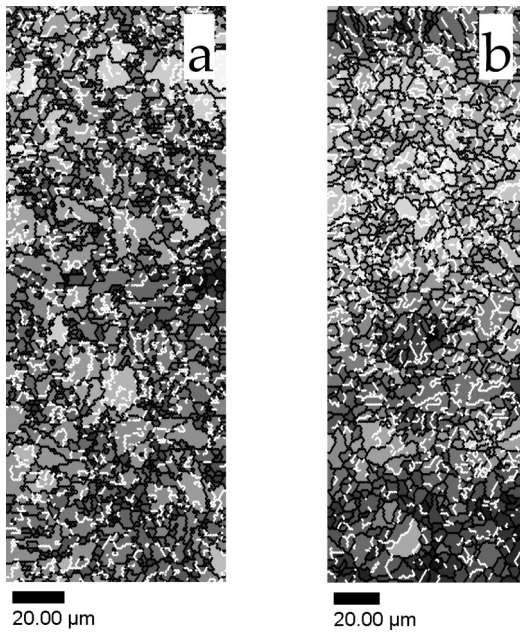

Fig. 7. EBSD investigations of (a) real and (b) simulated intercritical heat affected zones (T_{peak}=986°C).
White (resp. black) lines delineate low angle (5–15°) boundaries (resp. high-angle boundaries >15°).

the yield strength, but not on work hardening. The yield stress is 325 MPa at 5.10^{-3} s^{-1}, 280 MPa at 5.10^{-4} s^{-1} and 225 MPa at 5.10^{-5} s^{-1}. The tensile strength is 375 MPa at 5.10^{-3} s^{-1}, 330 MPa at 5.10^{-4} s^{-1} and 265 MPa at 5.10^{-5} s^{-1}. Whatever the strain rate, tensile curves exhibited a very low homogeneous elongation (<1%) before the onset of softening. Cross-section SEM examinations of the specimens with BSE channelling contrast and EBSD analysis showed strong modifications of the microstructure by dynamic recrystallisation, with highly misoriented grains of only a few hundreds of nanometers in mean size in the necking area. These results are similar to those obtained with the base metal.[48]

4.2. Creep flow properties at 625°C

Creep stress levels for NC5.0 specimens were set from
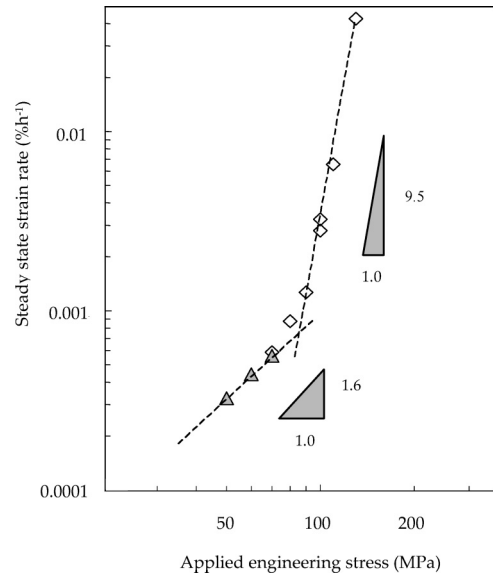

Fig. 8. Normalised steady state strain rate *versus* applied engineering stress.
(Open symbols=one test per load level, full symbols= multiple-steps test.)

130 to 70 MPa corresponding to creep lifetimes ranging between 150 h and 3 500 h. In addition, steady state creep strain rates at 50, 60, and 70 MPa were determined from the complementary test. The results of both kinds of tests at 70 MPa are nearly indistinguishable. Interpretation of these tests is not straightforward, as the notch induces multi-axial loading conditions. It requires inverse analysis by means of finite element calculations to determine the flow behaviour in a rigorous manner, which is out of scope of the present study. Here, the aim was to use a more simple representation to describe creep flow and damage behaviour of the ICHAZ. To do so, the concept of reference length, introduced by Yoshida[49] and Piques,[50] was used. It was assumed that deformation only occurs in the notched area over a length: $l_{ref} \approx l_{notch}$ where l_{notch}=6 mm for NC5.0 specimens. Therefore, overall steady state strain rates were evaluated with $\varepsilon = \Delta l / l_{ref}$ and plotted *versus* the applied engineering stress (**Fig. 8**). Two creep flow regimes can be identified, with a transition value for stress of about 80 MPa. In both regimes, the steady-state creep flow behaviour was represented using a Norton power-law, σ being the applied engineering stress and $\dot{\varepsilon}_{ss}$ the steady-state strain rate:

$$\dot{\varepsilon}_{ss} = B\sigma^n \quad ....(2)$$

The values of coefficients B and n were determined in both regimes:

1. For σ>70 MPa, deformation probably proceeds by dislocation climb or cross-slip with n=9.5 and B=2.13· 10^{-24} h^{-1} MPa$^{-9.5}$.
2. For σ<70 MPa, deformation probably proceeds by grain boundary diffusion with n=1.6 and B=5.75· 10^{-9} h^{-1} MPa$^{-1.6}$.

In the two creep regimes, the steady-state creep strain rates of the simulated ICHAZ are more than ten times higher than those encountered in the base metal.[51]
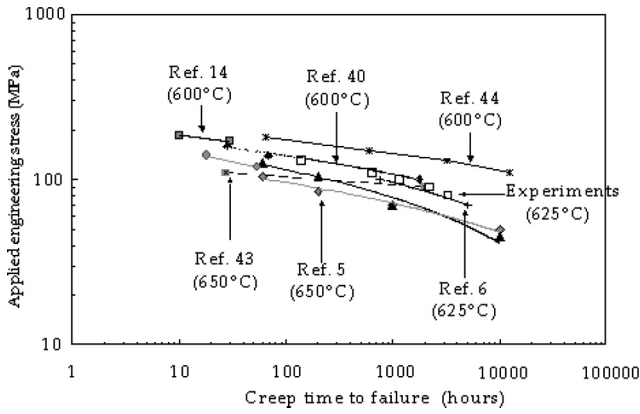
Fig. 9. Comparison of creep experiments on simulated ICHAZ at 625°C (NC5.0 specimens=open squares) with results from literature (smooth specimens).
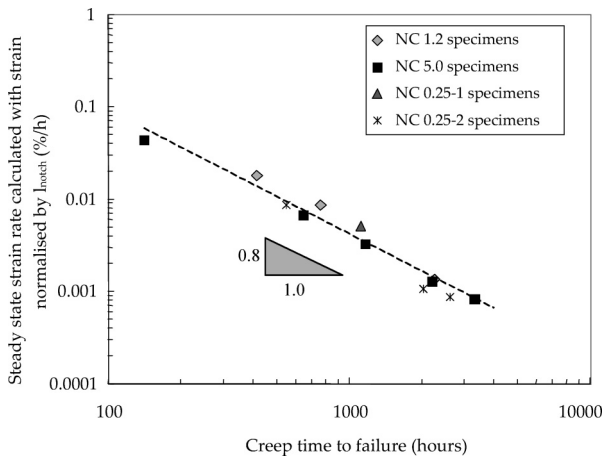

Fig. 10. Steady state strain rate *versus* time to failure for the simulated heat affected zone.

Fig. 11. Applied engineering stress *versus* creep time to failure for SC (cross-weld) and NC (simulated HAZ) specimens.

Fig. 12. EBSD maps of the damaged area of: (a) weldment (b) simulated HAZ specimens. Cavities are in black. White (resp. black) lines delineate low angle (5–15°) boundaries (resp. high-angle boundaries >15°).

4.3. Creep Fracture Properties

The experimental lifetime results of the present work are in good agreement with literature (**Fig. 9**). Literature data correspond to creep tests on smooth round specimens, which could explain that the results of the present study evidence a slightly better creep strength of the simulated HAZ due to the notch strengthening effect. To describe the creep fracture behaviour of the simulated ICHAZ, a Monkman–Grant (MG) relationship was used:

$$\dot{\varepsilon}_{ss}^{m} t_{R} = C_{MG} \quad \text{...............................(3)}$$

where m and C_{MG} are material parameters fitted in the high stress creep regime with $m=0.8$ and $C_{MG}=0.28h^{0.2}$, as no rupture data was available for the low stress creep regime. Using the concept of l_{ref}, a unique MG fit can predict creep failure for all kinds of specimen geometry (**Fig. 10**). Thus, the notch does not significantly affect the material ductility at least in the stress range experimentally investigated. Assuming that the material ductility remains constant, the MG fit was plotted in both high and low stress creep regimes (**Fig. 11**). Comparison with results on weldments (SC specimens) shows that predictions are in rather good agreement with experiments. MG predictions are a little optimistic in the high stress regime in comparison with tests on SC specimens (due to the notch strengthening effect) but are, on the contrary, conservative in the low stress regime.
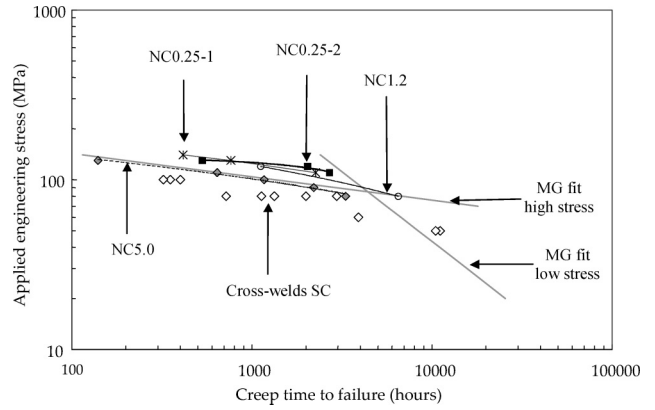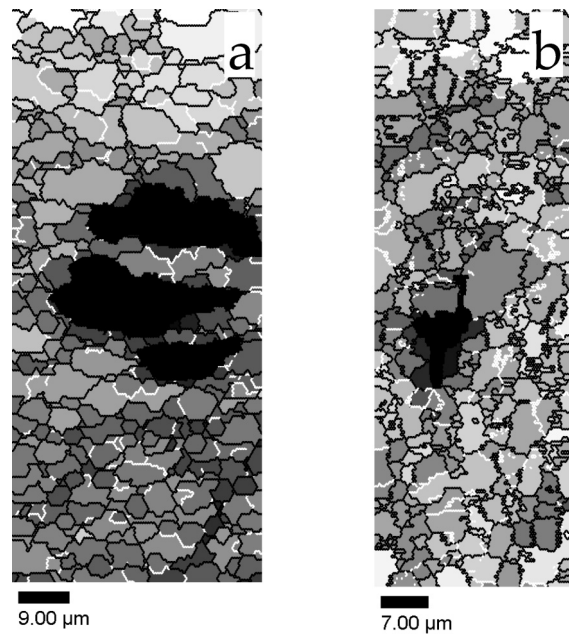
The evolution of the creep time to failure with stress is plotted in Fig. 11 for all specimens. A notch strengthening effect is evidenced for notch radii ranging from 5.0 to 1.2 mm. Note, however, that the strengthening effect is more limited between NC1.2 and NC0.25 specimens. Here, the high stress triaxiality ratio starts to markedly influence deformation and damage processes. In fact, the notch has a strengthening effect but it also shifts the transition between high and low stress creep regimes towards shorter creep lifetimes.[48]

4.4. Damage Mechanisms

Comparison between EBSD maps without creep (Fig. 7) and after creep (**Fig. 12**) shows that in both simulated and real HAZ microstructures, the fraction of high angle grain boundaries increases during creep. This indicates that even if the initial microstructure is totally recovered, softening further occurs during creep tests, possibly by recrystallisation.
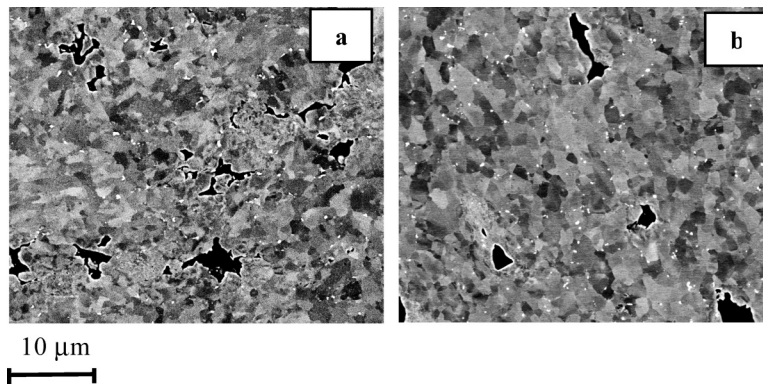
Fig. 13. Cross-section SEM observations of damage in specimens (a) weldment (b) simulated HAZ.
(Cavities in black and loading direction along the vertical axis.)

Cross-sections of creep fractured specimens (**Fig. 13**) show that similar damage mechanisms are encountered in weldments and in the simulated ICHAZ. This is confirmed by EBSD analysis (Fig. 12): in both materials, cavities mainly develop at high angle grain boundaries. They nucleate especially at grain boundary second phase particles such as Laves phases and $M_{23}C_6$ particles. Observations of carbon extraction replicas and EDS analysis performed in the FEG-SEM revealed the presence of numerous Laves phases larger than 300 nm. In both real and simulated ICHAZ microstructures, these precipitates largely promote cavity nucleation. The role of diffusion in cavity growth is predominant, which can be explained by a creep flow rate in the diffusion creep regime ten times faster in the simulated ICHAZ than in the base metal.

Both creep curves and damage investigations in notched simulated ICHAZ specimens can now be used to build, using inverse analysis with finite element simulation, a constitutive model coupling creep flow and damage as has already been done for the base metal.[48] This is the subject of a forthcoming paper.[52]

5. Conclusions

In the present study, attention was focused on determining the creep flow and damage properties of the weakest zone of 9Cr1Mo–NbV steel weldments using various kinds of specimen geometry and multi-scale metallurgical investigations. The following conclusions can be drawn:

(1) 9Cr1Mo–NbV weldments exhibit a strong drop in creep strength in comparison with the base metal. This drop is attributed to the lower creep strength of the ICHAZ.

(2) A thermal model was fitted and used to satisfactorily represent various microstructural areas of the HAZ. A weld thermal cycle leading to the formation of a microstructure having the same properties as the weakest HAZ was identified based on both metallurgical and mechanical investigations. The peak temperature (986°C) of this thermal treatment is in the upper bound of the intercritical domain, for the chosen heating rate of $155°C \cdot s^{-1}$.

(3) Mechanical tests on the simulated microstructure, with controlled stress triaxiality effects, show that the ICHAZ intrinsically exhibits a higher creep rate responsible for its creep strength being lower than that of the base metal.

REFERENCES

1) R. L. Klueh and D. R. Harries: High-Chromium Ferritic and Martensitic Steels for Nuclear Applications, American Society for Testing and Materials, West Conshohocken, PA, (2001), 71.
2) J. Brozda and M. Zeman: *Weld. Int.*, **10** (1996), 370.
3) A. Jakobová, V. Vodárek, K. Hennhofer and V. Foldyna: Proc. of the Sixth Liège Conf. on Materials for Advanced Power Engineering, Energy Technology Series Vol. 5, ed. by J. Lecomte-Beckers, F. Schubert, P. J. Ennis, Forschungszentrum Jülich GmbH, Jülich, Germany, (1998), 373.
4) M. DeWitte and C. Coussement: *Mater. High Temp.*, **9** (1991), 178.
5) Y. Otoguro, M. Matsubara, I. Itoh and T. Nakazawa: *Nucl. Eng. Des.*, **196** (2000), 51.
6) Y. Tsuchida, K. Okamoto, Y. Tokunaya: *Weld. Int.*, **10** (1996), 454.
7) A. Danon, C. Servant, A. Alamo and J. C. Brachet: *Mater. Sci. Eng. A*, **A348** (2003), 122.
8) D. Rosenthal: *Weld. J.*, **20** (1941), 220s.
9) N. N. Rykalin: Calculation of Heat Flow in Welding, Verlag Technik, Berlin, (1957), 45.
10) O. R. Myhr and Ø. Grong: *Acta Metall. Mater.*, **38** (1990), 449.
11) J. Warreing: CEA/SRMA, Internal Report N.T SRMA94-2013, (1994).
12) K. Haarmann, J. C. Vailant, W. Bendick and A. Anbab: The T91/P91 Book, Vallourec & Mannesmann Tubes, (1999).
13) L. F. Alvarez and C. Garcia: *Rev. Metall.*, *Cah. Inf. Tech.*, **92** (1995), 247, 1411.
14) H. Cerjak and F. Schuster: Second Conf. on Joining Technology EUROJOIN 2. Istituto Italiano della Saldatura, Genova, Italy, (1994), 157.
15) R. K. Shiue, K. C. Lan and C. Chen: *Mater. Sci. Eng.*, **A287** (2000), 10.
16) V. Moorthy, S. Vaidyanathan, K. Laha, T. Jayakumar, V. Bhanu Sankara Rao and B. Raj: *Mater. Sci. Eng.*, **A231** (1997), 98.
17) J. C. Brachet: *Journal de Physique IV* (*France*)—*Colloque C8*, **5** (1995), C8-339.
18) M. Taneike, K. Sawada and F. Abe: *Metall. Trans. A*, **35A** (2004), 1255.
19) J. Orr and A. Di Francesco: *Ironmaking Steelmaking*, **20** (1993), 424.
20) T. Kojima, K. Hagashi and T. Kajita: *ISIJ Int.*, **35** (1995), 1284.
21) T. Akbay, R. C. Reed, and C. Atkinson: *Acta Metall. Mater.*, **47** (1994), 1469.
22) J. C. Brachet: PhD Thesis, Paris Sud Orsay University, (1991), (in French).
23) Z. K. Liu, L. Hoglund, B. Jonsson and J. Agren: *Metall. Trans. A*,

22A (1991), 1753.

24) J. Agren and G. Vassilev: *Mater. Sci. Eng.*, **64** (1984), 95.

25) D. V. Shantsky and G. Inden: *Acta Mater.*, **45** (1997), 2879.

26) S. J. Sanderson: *Met. Sci.*, **12** (1978), 220.

27) C. S. Roberts: *Trans. Metall. Soc. AIME*, **197** (1953), 203.

28) P. J. Winchell and M. Cohen: *Trans. Am. Soc. Met.*, **55** (1962), 347.

29) W. Bendick, K. Niederhoff, G. Wellnitz, M. Zschau and H. Cerjak: Third Int. Conf. on Trends in Welding Research, ed. by S. A. David, J. M. Vitek, ASM International, Metals Park, OH, (1992) 587.

30) M. Vijayalakshmi, S. Saroja, V. Thomas Paul, R. Mythili and V. S. Raghunathan: *Metall. Mater. Trans. A*, **30A** (1999), 161.

31) T. Nakajima, S. Spigarelli, E. Evangelista and T. Endo: *Mater. Trans.*, **44** (2003), No. 9, 1802.

32) M. Hättestrand and H. O. Andrén: *Acta Mater.*, **49** (2001), 2123.

33) E. Cerri, E. Evangelista, S. Spigarelli and P. Bianchi: *Mater. Sci. Eng.*, **A245** (1998), 285.

34) S. L. Tian, C. Coussement, M. DeWitte and M. Shee: *Int. J. Pressure Vessels Piping*, **46** (1991), 339.

35) T. Tsuchiyama, T. Miyamoto and S. Takaki: *ISIJ Int.*, **41** (2001), 1047.

36) S. Spigarelli and E. Quadrini: *Mater. Des.*, **23** (2002), 547.

37) S. K. Albert, M. Matsui, T. Watanabe, H. Hongo, K. Kubo and M. Tabuchi: *ISIJ Int.*, **42** (2002), 1497.

38) J. Hald and E.M. Lund: Int. Conf. on the Joining of Materials JOM-6, ed. by O. Al-Erhayem, The European Institute for the Joining of Materials, DTU Helsingør, Denmark, (1993), 317.

39) H. Cerjak, E. Letofsky, F. Schuster: Fourth Int. Conf. on Trends in Welding Research, ASM International, Metals Park, OH, (1995), 1633.

40) G. Eggeler, A. Ramteke, M. Coleman, A. Burblies, G. Peter, J. Hald, C. Jefferey, J. Rantala, M. DeWitte and R. Mohrmann: *Int. J.*

Pressure Vessels Piping, **60** (1994), 237.

41) S.K. Albert , M. Matsui, T. Watanabe, H. Hongo, K. Kubo and M. Tabuchi: *ISIJ Int.*, **42** (2002), 1497.

42) H. Cerjak, E. Letofsky, R. Hanus, H. Heuser and C. Jochum: PARSONS 2000: Parsons 2000 Advanced Materials for 21st Century Turbines and Power Plant, ed. by A. Strang, W. M. Banks, R. D. Conroy, G. M. McColvin, J. C. Neal and S. Simpson, IOM, London, (2000) 386.

43) M. Matsui, M. Tabuchi, T. Watanabe, K. Kubo, J. Kinugawa and F. Abe: *ISIJ Int.*, **41** (2001), s126.

44) R.Wu, R. Sandstrom and F. Seitisleam: *J. Eng. Mater. Technol.* (*Trans. ASME*), **126** (2004), 87.

45) A. J. Murdoch, D. J. Allen and S. G. R. Brown: Proc. Baltica V—Condition and Life Management for Power Plants, vol. 1, ed. by S. Hietanen and P. Auerkari, Technical Research Centre of Finland (VTT), Espoo, Finland, (2001), 263.

46) K. Laha, K. S. Chandravathi and K. Bhanu Sankara Rao: *Trans. Indian Inst. Met.*, **53** (2000), 217.

47) G. Eggeler, J. C. Earthmann, N. Nilsvang and B. Ilschner: *Acta Metall.*, **37** (1989), 49.

48) V. Gaffard, J. Besson and A. F. Gourgues-Lorenzon: *Int. J. Fract.*, **133** (2005), 139.

49) M. Yoshida: PhD Thesis, Ecole Nationale Supérieure des Mines de Paris, Paris, France (in French), (1985).

50) R. Piques: PhD Thesis, Ecole Nationale Supérieure des Mines de Paris, Paris, France (in French), (1989).

51) L. Kloc and V. Sklenička: *Mater. Sci. Eng.*, **A234-236** (1997), 962.

52) V. Gaffard, J. Besson and A. F. Gourgues-Lorenzon: Proc. of ECCC Conf. on Creep and Fracture in High Temperature Components, ed. by I. A. Shibli, S. R. Holdsworth and G. Merckling, Destech Publications, Lancaster, PA, (2005), 58.